Supporting Information

Chemically bonded and plasmonic Z-scheme junction for high-performance artificial photosynthesis of hydrogen peroxide

Teng Shao, Yuan Chang, Zhuwei Li, Yurou Song, Dingfeng Jin, Junfeng Gao, Licheng Sun and Jungang Hou*

T. Shao, Z. Li, Y. Song, D. Jin, Prof. Dr. J. Hou,
State Key Laboratory of Fine Chemicals, Frontiers Science Center for Smart Materials Oriented Chemical Engineering, School of Chemical Engineering, Dalian University of Technology, Dalian 116024, P. R. China. E-mail: jhou@dlut.edu.cn

Y. Chang, Prof. Dr. J. Gao
Laboratory of Materials Modification by Laser, Ion and Electron Beams, Ministry of Education, Dalian University of Technology, Dalian 116024, P. R. China.

Prof. Dr. L. Sun
Center of Artificial Photosynthesis for Solar Fuels and Department of Chemistry, School of Science, Westlake University, Hangzhou 310024, P. R. China.

Prof. Dr. L. Sun
School of Engineering Sciences in Chemistry, Biotechnology and Health, Department of Chemistry, KTH Royal Institute of Technology, 10044 Stockholm, Sweden.

Chemicals

Melamine ($C_3H_6N_6$, 99%), Tungsten chloride (WCl_6, 99%), Cerium (IV) sulfate ($Ce(SO_4)_2$, 99.9%), Isopropanol (C_3H_8O, 99.7%), were purchased from Shanghai Aladdin Bio-Chem Technology Co., Ltd. High purity N_2 (99.999%) and O_2 (99.999%) were purchased from Dalian Guang Ming Special Gas Products Co., Ltd. Absolute ethanol, deionized water and all chemicals were used without any purification for this work.

Synthesis of CN/WO-X heterostructures

Bulk g-C_3N_4 and carbon nitride nanosheets were synthesized according to the previous literature.[1,2] g-C_3N_4/$W_{18}O_{49}$ heterostructures (CN/WO-X) were synthesized according to the previous literature.[3] The final product was freeze-dried and ground to obtain CN/WO-X (X is the mass ratio of WO). Pure WO was synthesized under the same conditions as above except for CN.

Characterization

SEM images of samples were captured by a field-emission scanning electron microscopy (SEM, FEI Nova Nano SEM 450). TEM images of the samples were performed on transmission electron microscopy (TEM, FEI TF30). XRD patterns of the samples were tested by X-ray diffractometer (Japan Rigaku Rotaflex) with Cu Kα radiation (λ = 1.5418 nm, 40 kV, 40 mA) at room temperature. The Fourier transform infrared (FT-IR) spectra were acquired on a FT-IR spectrometer in KBr tablets, at room temperature (Shimadzu Corp). X-ray photoelectron spectroscopy (XPS, ESCALAB 250) was applied to reveal the elements composition and valence states of materials. UV-vis absorption was measured by UV-vis-NIR spectrophotometer (Shimadzu UV-3600 Plus). Photoluminescence (PL) spectra were measured by fluorescence spectrometer (Horiba, FloroMax-4P). Time-resolved photoluminescence tests of the samples were conducted by transient

steady-state fluorescence spectrometer (Edinburgh Instruments FLS1000). Electron paramagnetic resonance (EPR) tests were performed under ambient room temperature through Bruker 500 spectrometer (Bruker A200). The femtosecond transient absorption (TA) spectra were measured by optical pump-probe spectroscopy with a modelocked Ti-sapphire laser amplifier (Spectra-Physics) as the source of femtosecond radiation.

Theoretical calculations

Density functional theory (DFT) calculations are implemented by VASP 6.3.0 code.[4,5] We utilize Perdew-Burke-Ernzerhof (PBE) method of generalized gradient approximation (GGA) functional to describe the exchange and correlation interaction.[6-8] During self-consistent field calculations, the following valence electron were induced: H ($1s^1$), C ($2s^2$ and $2p^2$), N ($2s^2$ and $2p^3$), O ($2s^2$ and $2p^4$) and W ($6s^2$ and $5d^4$). Spin-polarization is restricted without magnetism, but released during the calculation of singlet state and triplet state oxygen. We adopt two-dimensional g-C_3N_4 (7.135 Å×12.358 Å×7.138 Å, γ=90°) and $W_{18}O_{49}$ (14.199 Å×18.287 Å×3.859 Å, γ=70.29°) to generate the CN/WO heterostructures. An adequate vacuum layer of 20 Å is set to prevent the periodic effect. Correspondingly, the 2×2×1 k-mesh is utilized for monolayer and bilayer model. The cutoff energy is set to be 400 eV. The criteria of energy convergence and force convergence are set to 10^{-5} eV and 0.01 eV/ Å. All the numerical accuracy has been carefully tested.

The oxygen reduction reaction (ORR) can be described as following $2e^-$ processes to hydrogen peroxide.[9]

$$* + O_2\,(g) \rightarrow *O_2 \qquad (1\text{-}1)$$

$$*O_2 + H^+ + e^- \rightarrow *O_2 + *H \qquad (1\text{-}2)$$

$$*O_2 + *H \rightarrow *OOH \qquad (1\text{-}3)$$

$$*OOH + H+ + e^- \rightarrow *H_2O_2 \quad (1\text{-}4)$$

$$*H_2O_2 \rightarrow * + H_2O_2 \quad (1\text{-}5)$$

According to above equations, the catalytic performance of configurations can be evaluated by free energy ΔG which is defined as:

$$\Delta G = E_{ads} + \Delta E_{ZPE} - T\Delta S$$

where ΔE_{ZPE} represents the vibrations of all degrees of freedom of adsorbates under the harmonic approximation, T and ΔS are temperature and entropy change, respectively.

Photocatalytic tests

CN/WO heterostructures with photocatalytic oxygen reduction for hydrogen peroxide production were tested at room temperature. In a typical experiment, 50 mg of photocatalyst was put in a sealed Schlenk bottle and added to 25 mL of solution (Volume ratio of deionized water to isopropanol is 9:1). Ultrasonic agitation 20 minutes to fully disperse, pure oxygen was introduced in the dark place for 30 min and stirred continuously, a 300W Xe lamp with AM 1.5G (λ>420 nm) as light source. The solution was sampled using a 5 mL syringe at certain time intervals, and the photocatalyst was removed using a filter with a 0.22 μm filter membrane, and H_2O_2 was detected by UV-vis absorption spectroscopy. For the determination of H_2O_2, cerium sulfate titration method was used. The reaction equation is as follows:

$$2Ce^{4+} + H_2O_2 \rightarrow 2Ce^{3+} + 2H^+ + O_2$$

The yellow solution based on Ce^{4+} would be reduced to colorless Ce^{3+}, and Ce^{4+} has strong UV-vis absorption at 318 nm.[10] The concentration of H_2O_2 is determined by plotting the standard curve.

Photoelectrochemical (PEC) tests

PEC tests were performed on a CHI 660E electrochemical workstation equipped with a three-electrode cell. A homogeneous slurry consisting of 5 mg of photocatalyst, 20 μl of 5wt% nafion solution, 550 μl of absolute ethanol, and 450 μl of deionized water was suspended onto FTO glasses as the working electrode. The counter electrode was Pt, and the reference electrode was a saturated Ag/AgCl electrode with 0.2 M Na_2SO_4 (pH=6.8) electrolyte. A 300 W Xe lamp with AM 1.5G (λ > 420 nm, 100 mW cm^{-2}) was used as light source. The I-T curves were tested under switching light conditions. Electrochemical impedance spectroscopy (EIS) measurements were performed in the frequency range of 0.1 Hz -10^5Hz. The Mott-Schottky (M-S) plots of the photocatalysts with the same three-electrode system were obtained at frequencies of 500, 1000 and 1500 Hz. All the potentials versus reversible hydrogen potential (RHE) were converted from the potentials versus Ag/AgCl according to the Nernst equation:

$$E_{RHE} = E_{Ag/AgCl} + 0.059\ pH + 0.197$$

where E_{RHE} refers to the converted potential versus RHE. The $E_{Ag/AgCl}$ is the obtained potential versus Ag/AgCl, and pH was the pH value of electrolyte.

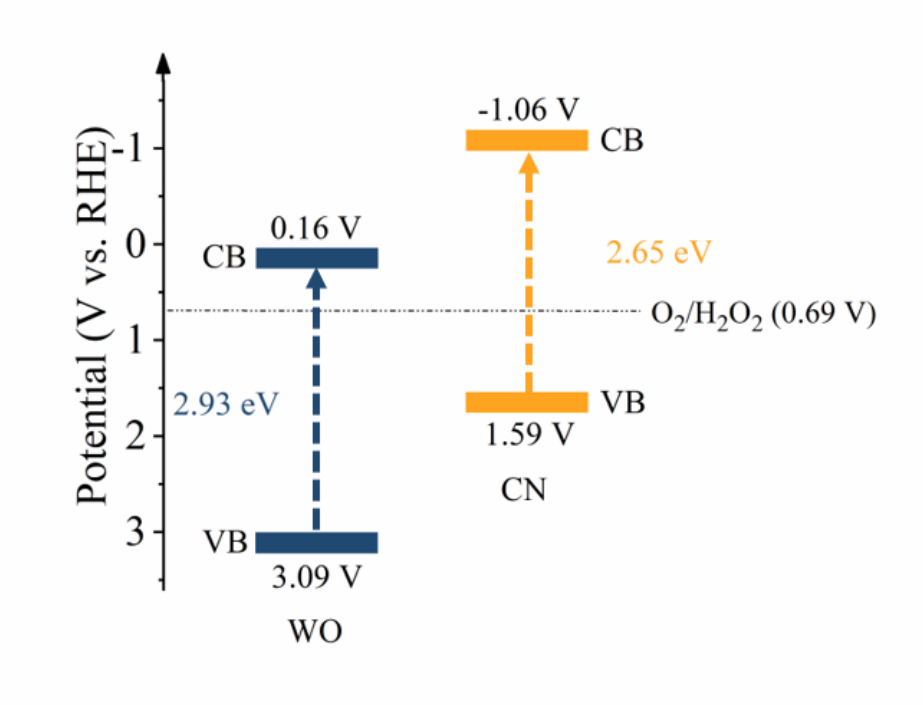

Fig. S1 Energy band alignment of WO and CN.

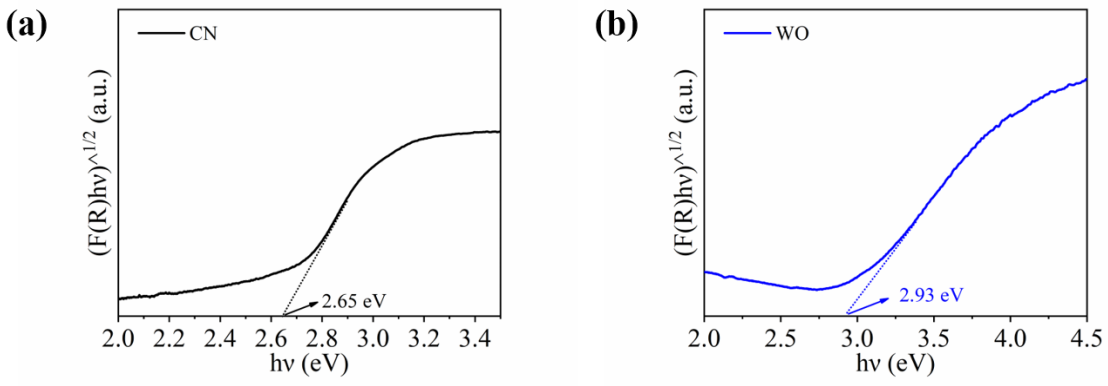

Fig. S2 Tauc plots of (a) CN and (b) WO. The band gap (E_g) of CN and WO is estimated to be 2.65 eV and 2.93 eV by Tauc plot, respectively.

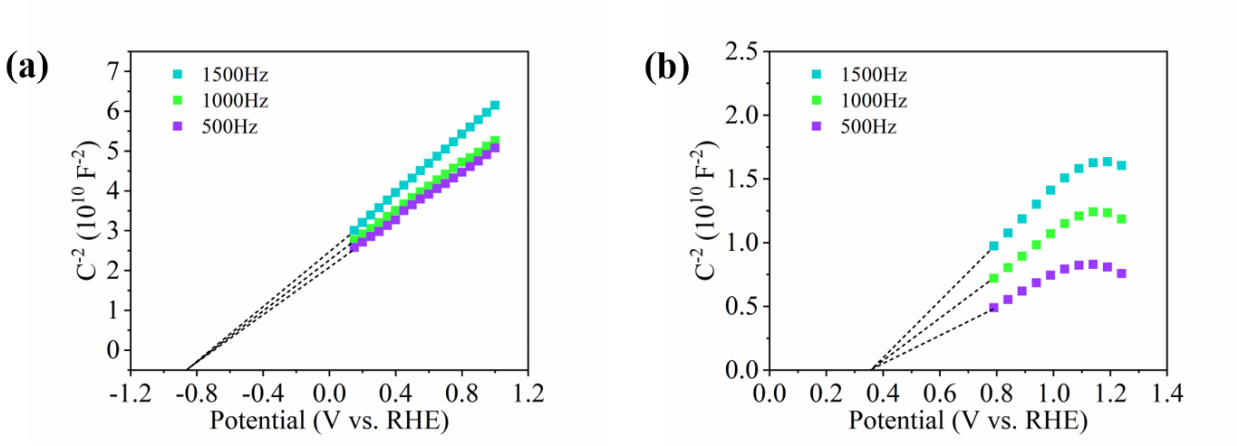

Fig. S3 Mott-Schottky plots of (a) CN and (b) WO. From the Mott-Schottky curves at different frequencies from 500 to 1500 Hz, the flat band potential obtained by the intercept of the tangents on the x-axis. The Mott-Schottky curves possess the positive slope.[11]

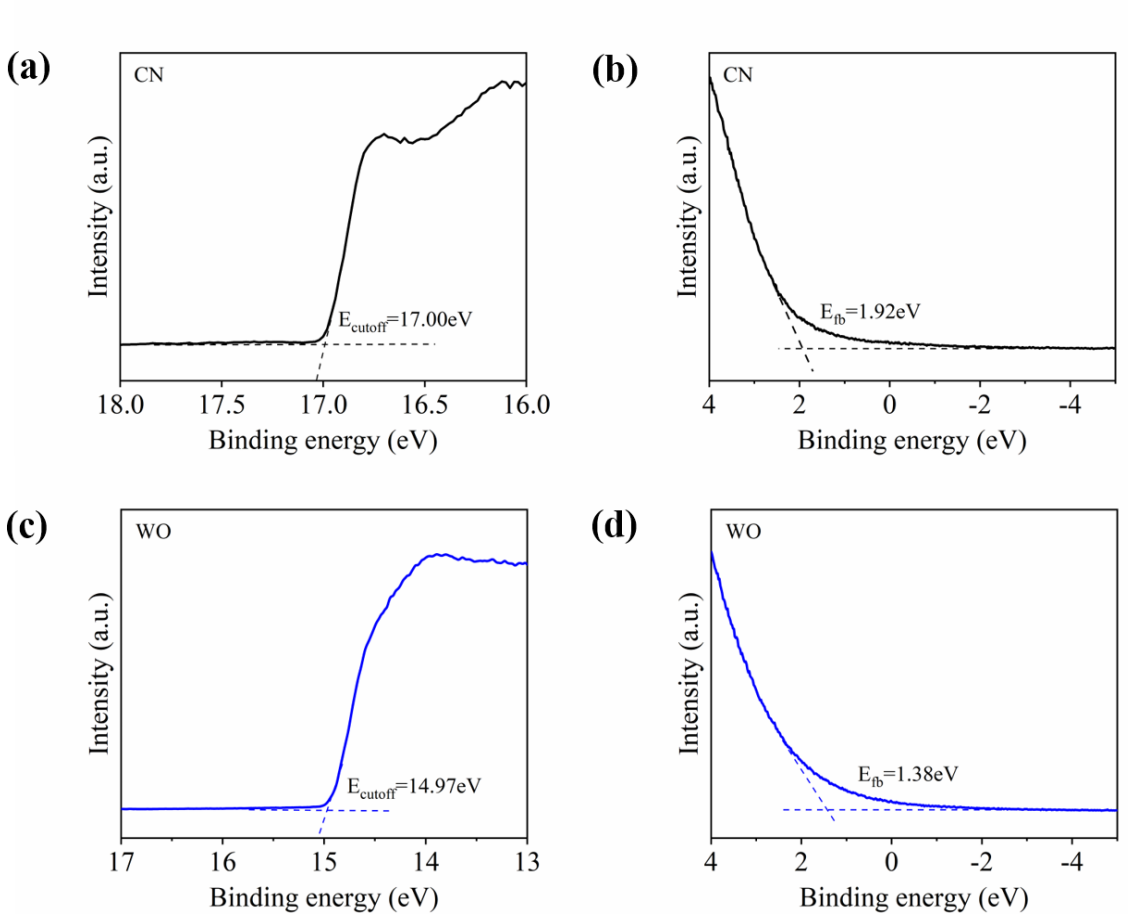

Fig. S4 Ultraviolet photoelectron spectroscopy (UPS) spectrum of CN and WO. Secondary electron cutoff for (a) CN and (c) WO, and Fermi band for (b) CN and (d) WO. To further elucidate the energy band structure of CN and WO, the secondary electron cutoff and Fermi band were studied by UPS spectra.[12] Based on the UPS analysis, the valence bands (VB) of CN and WO were basically consistent with the above analysis.

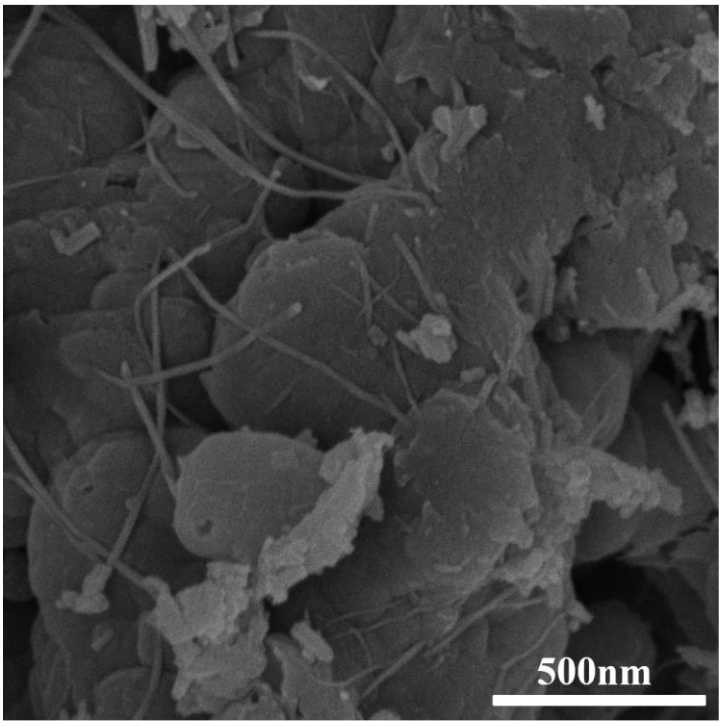

Fig. S5 SEM of CN/WO-12.5% heterostructure.

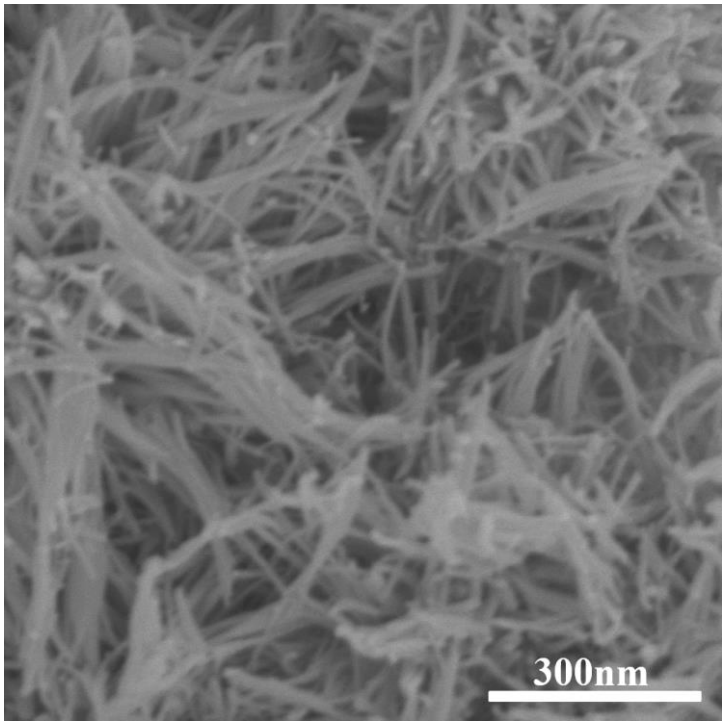

Fig. S6 SEM of pure WO nanowires.

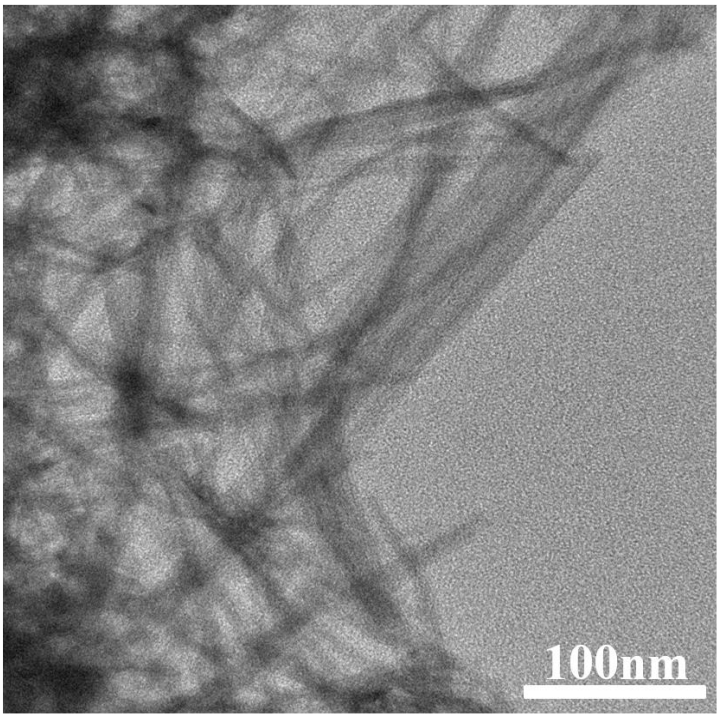

Fig. S7 TEM image of pure WO nanowires.

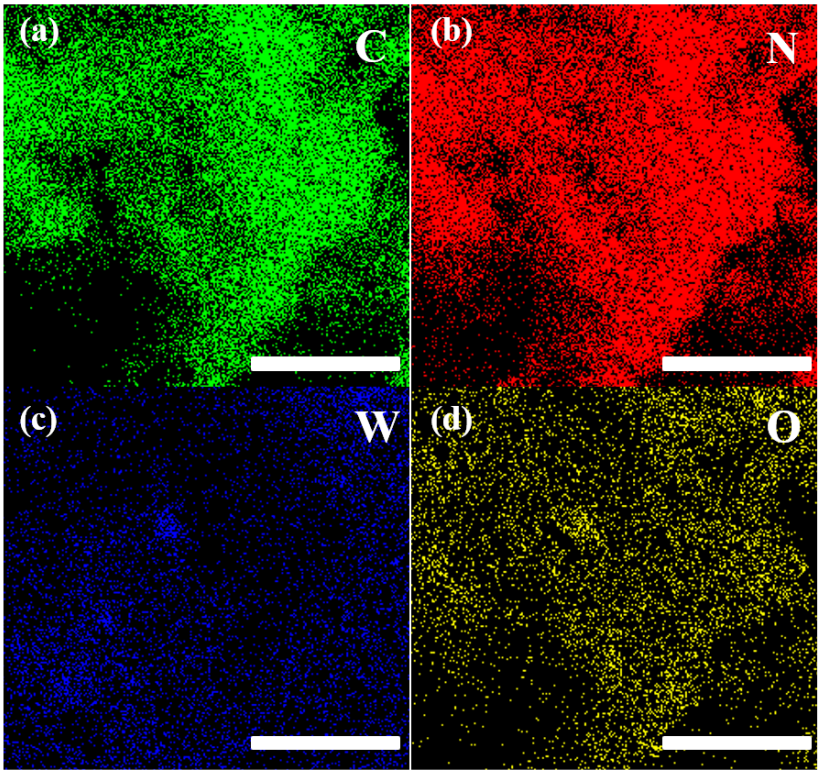

Fig. S8 Element mappings of CN/WO-12.5% heterostructure.

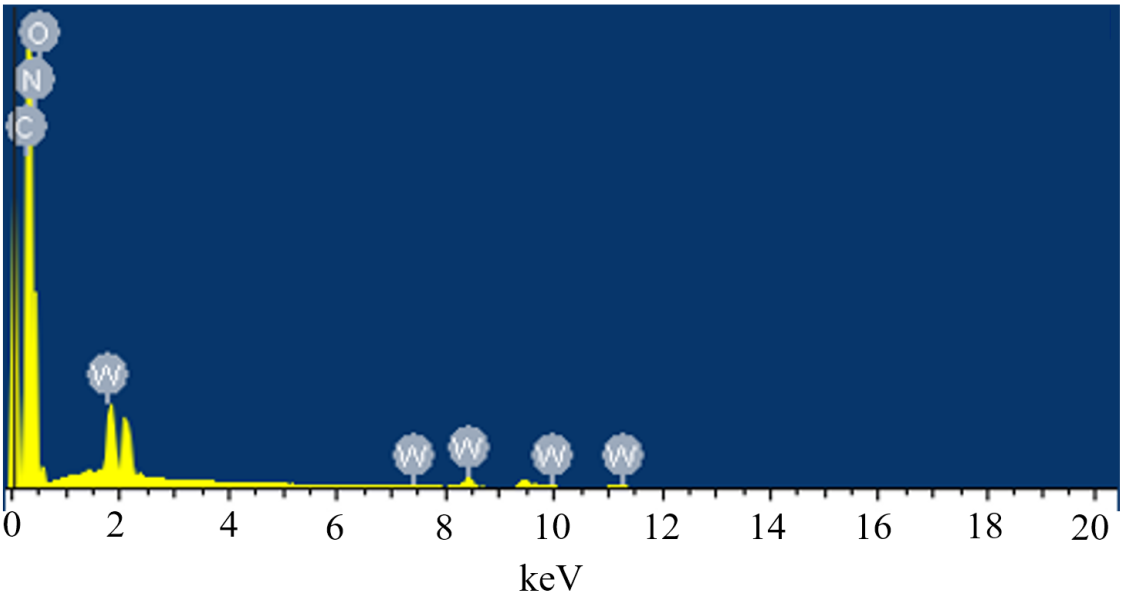

Fig. S9 EDS spectrum of CN/WO-12.5% heterostructure.

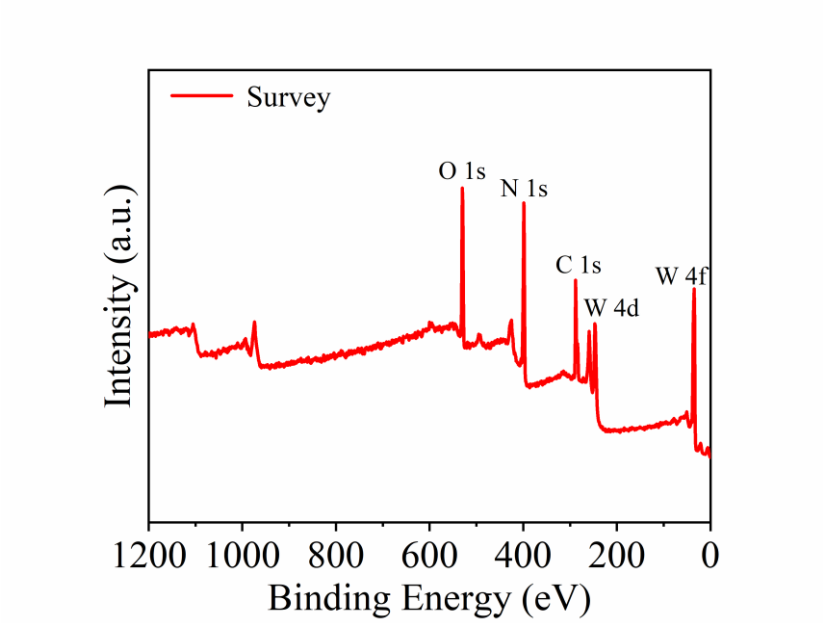

Fig. S10 Full survey XPS spectra of CN/WO-12.5% heterostructure.

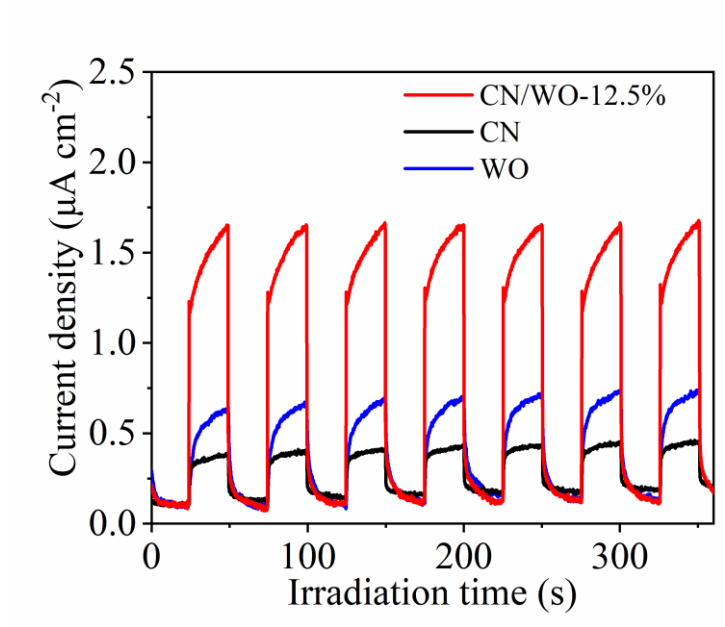

Fig. S11 Transient photocurrent responses of CN, WO, CN/WO-12.5% heterostructure.

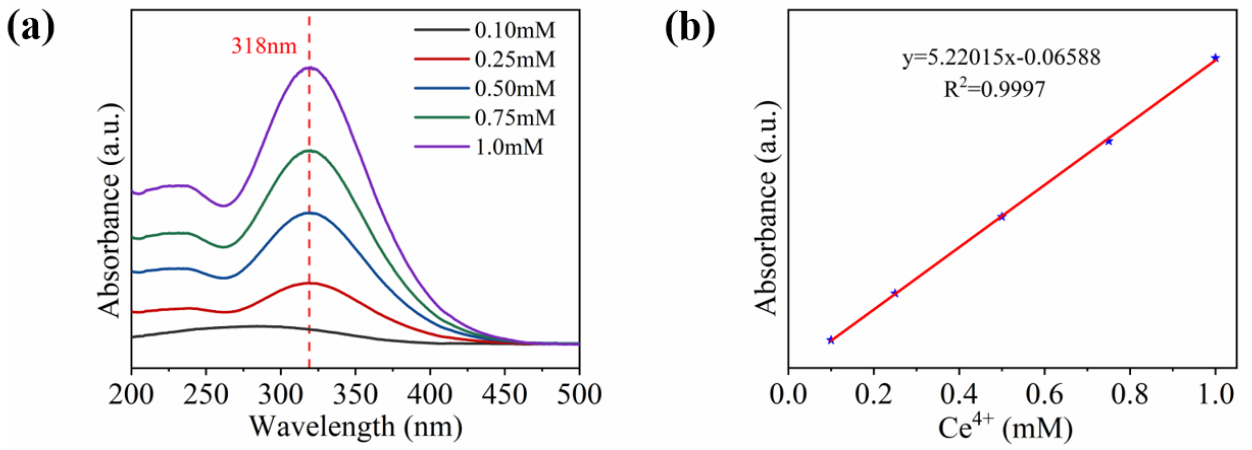

Fig. S12 Determination of hydrogen peroxide concentration. (a) UV-vis absorption spectra of standard solutions of different concentrations of Cerium sulfate at room temperature. (b) Standard curve for the concentration of $Ce(SO_4)_2$ solution.

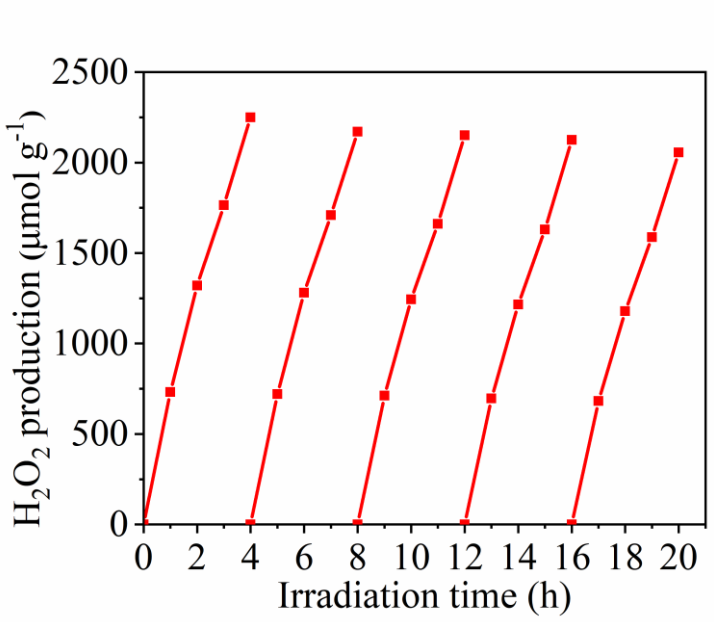

Fig. S13 Recycling photocatalytic stability tests of hydrogen peroxide production for CN/WO-12.5% heterostructure under visible-light irradiation (λ >420 nm).

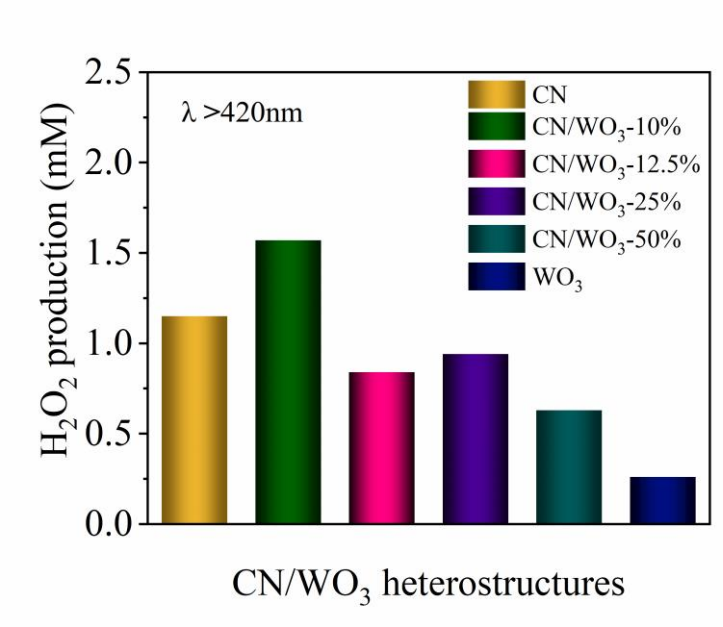

Fig. S14 Photocatalytic hydrogen peroxide production for CN/WO heterostructures after sufficient calcination in air under visible-light irradiation (λ >420 nm) for 4 h.

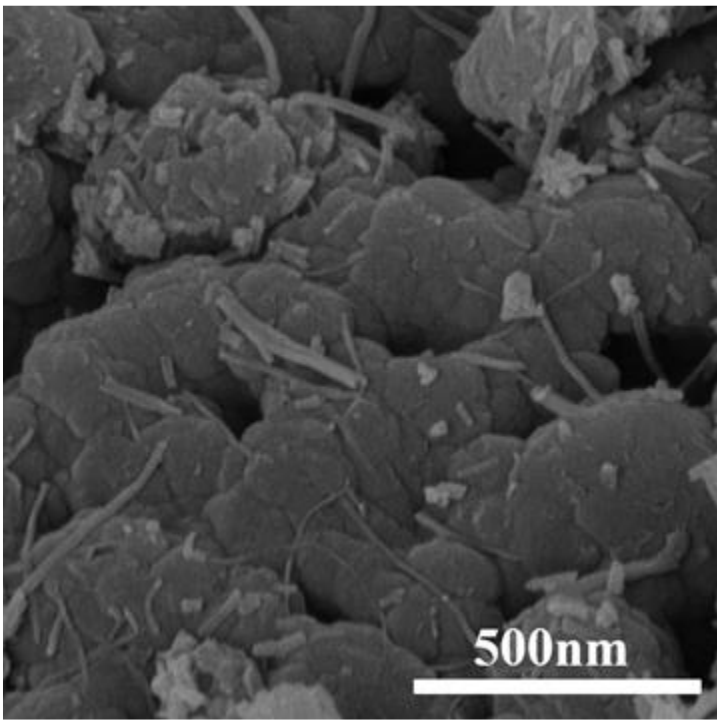

Fig. S15 SEM of CN/WO-12.5% heterostructure after the reaction.

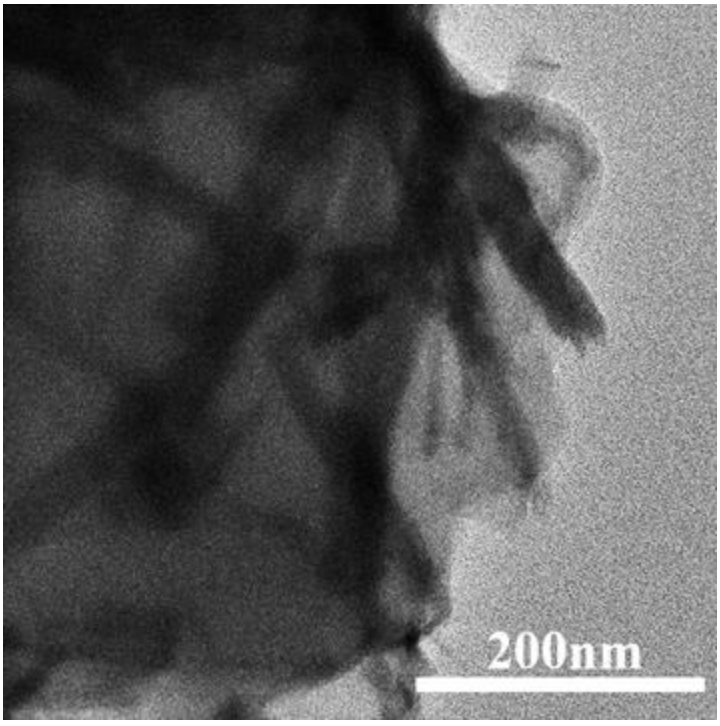

Fig. S16 TEM of CN/WO-12.5% heterostructure after the reaction.

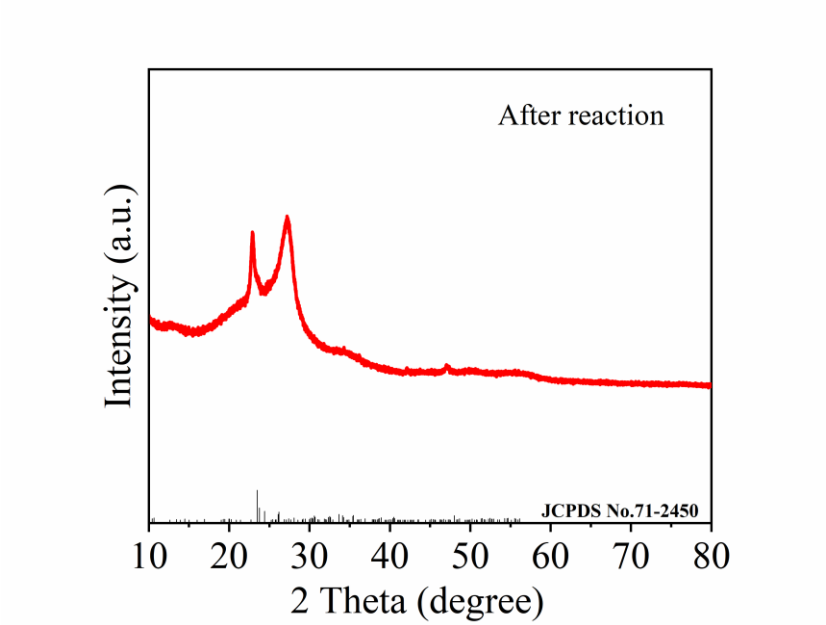

Fig. S17 XRD of CN/WO-12.5% heterostructure after the reaction.

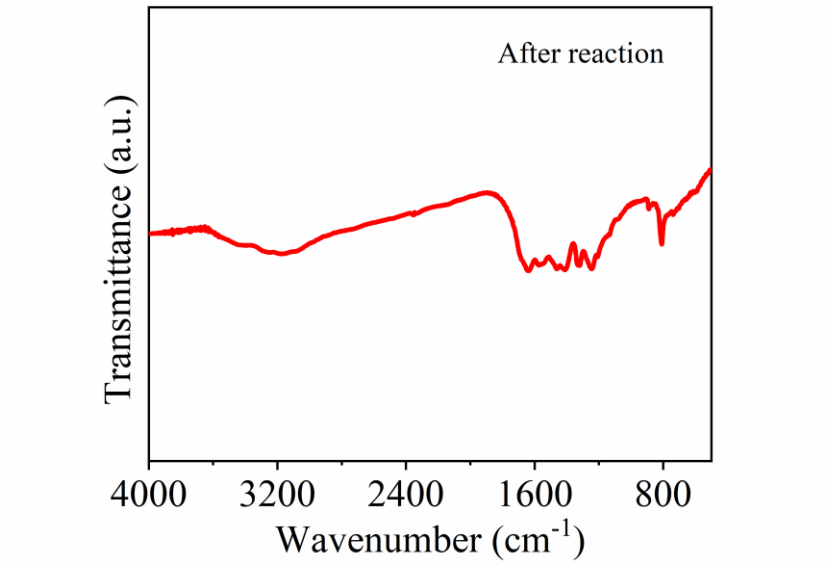

Fig. S18 FT-IR of CN/WO-12.5% heterostructure after the reaction.

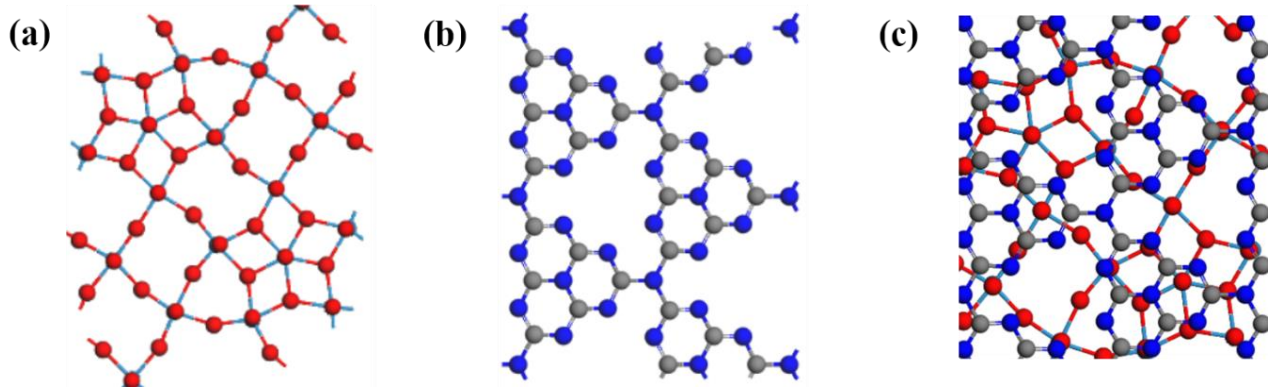

Fig. S19 Structures models of (a) CN, (b) WO and CN/WO heterostructures. Cyan, red, gray and blue balls denote tungsten, oxygen, carbon and nitrogen atoms, respectively.

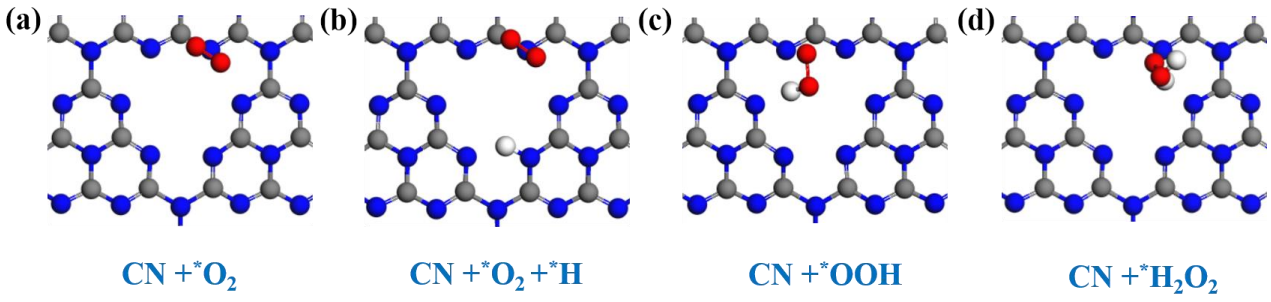

Fig. S20 Adsorption models of reaction intermediates of (a) CN +$^*O_2$, (b) CN +$^*O_2$ +*H, (c) CN +*OOH, (d) CN +$^*H_2O_2$. Red and white balls denote oxygen and hydrogen atoms, respectively.

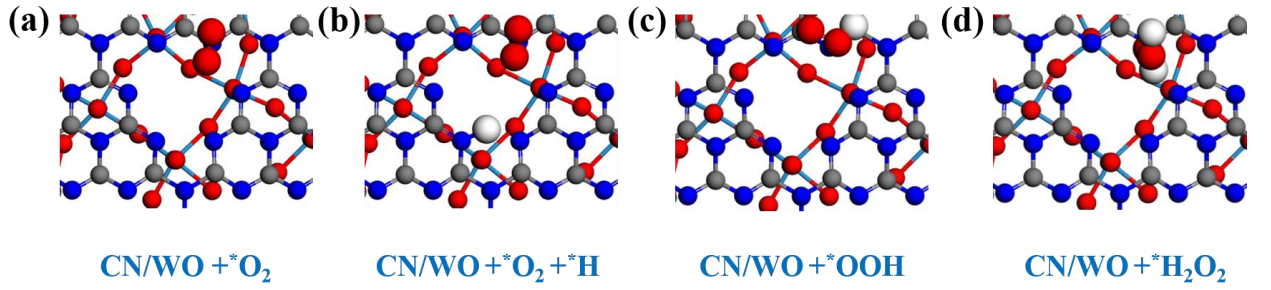

Fig. S21 Adsorption models of reaction intermediates of (a) CN/WO +$^*O_2$, (b) CN/WO +$^*O_2$ +*H, (c) CN/WO +*OOH, (d) CN/WO +$^*H_2O_2$. Red and white balls denote oxygen and hydrogen atoms, respectively.

Table S1. The fitting parameters of time-resolved transient photoluminescence (TRPL) for CN and CN/WO-12.5% with excitation at 350 nm.

Photocatalysts	λ_{ex} (nm)	τ_1(ns)	A_1(%)	τ_2(ns)	A_2(%)
CN/WO-12.5%	350	3.16	94.22%	20.66	5.78%
CN	350	1.82	80.61%	8.59	19.39%

Table S2. The fitting parameters of transient absorption (TA) for CN and CN/WO-12.5% for the excitation at 400 nm and detection at 600 nm.

Photocatalysts	λ_{ex} (nm)	λ_{probe} (nm)	τ_1(ps)	A_1(%)	τ_2(ps)	A_2(%)	τ_{avg}(ps)
CN/WO-12.5%	400	600	16.79	41.59%	309.39	58.41 %	298.50
CN	400	600	4.67	44.32%	120.26	55.68 %	116.79

Table S3. Detailed adsorption energy (E_{ads}), zero point energy (ΔE_{ZPE}), entropy contribution ($T\Delta S$) and free energy (ΔG) of pristine CN under 0 e/Å electric field in ORR process (Unit: eV). Energy of H_2 and H_2O are calculated to be -6.763 eV and -14.233 eV.

Adsorbate	E_{total}	E_*	E_{ads}	ΔE_{ZPE}	$T\Delta S$	ΔG (U=1.23 V)
$*+O_2$	-486.755	-475.105	-	-	-	0
$*O_2$	-485.648	-475.105	4.397	0.24	0.057	1.29
$*O_2+*H$	-489.778	-475.105	3.649	0.573	0.046	0.486
*OOH	-490.275	-475.105	3.152	0.532	0.076	-0.082
$*H_2O_2$	-495.425	-475.105	1.383	0.868	0.082	-0.291

Table S4. Detailed adsorption energy (E_{ads}), zero point energy (ΔE_{ZPE}), entropy contribution ($T\Delta S$) and free energy (ΔG) of CN/WO under 0 e/Å electric field in ORR process (Unit: eV).

Adsorbate	E_{total}	E_*	E_{ads}	ΔE_{ZPE}	$T\Delta S$	ΔG (U=1.23 V)
$*+O_2$	-1258.392	-1247.021	-	-	-	0
$*O_2$	-1257.658	-1247.021	4.303	0.138	0.181	0.734
$*O_2+*H$	-1261.914	-1247.021	3.429	0.414	0.213	-0.06
*OOH	-1262.275	-1247.021	3.068	0.517	0.075	-0.18
$*H_2O_2$	-1267.41	-1247.021	1.314	0.812	0.165	-0.499

Table S5. Detailed adsorption energy (E_{ads}), zero point energy (ΔE_{ZPE}), entropy contribution ($T\Delta S$) and free energy (ΔG) of CN/WO under 0.2 e/Å electric field in ORR process (Unit: eV).

Adsorbate	E_{total}	E_*	E_{ads}	ΔE_{ZPE}	$T\Delta S$	ΔG (U=1.23 V)
$*+O_2$	-1258.762	-1247.33	-	-	-	0
$*O_2$	-1258.081	-1247.33	4.303	0.138	0.181	0.681
$*O_2+*H$	-1262.281	-1247.33	3.429	0.414	0.213	-0.118
*OOH	-1262.668	-1247.33	3.068	0.517	0.075	-0.264
$*H_2O_2$	-1267.715	-1247.33	1.314	0.812	0.165	-0.495

Table S6. Detailed adsorption energy (E_{ads}), zero point energy (ΔE_{ZPE}), entropy contribution ($T\Delta S$) and free energy (ΔG) of CN/WO under 0.4 e/Å electric field in ORR process (Unit: eV).

Adsorbate	E_{total}	E_*	E_{ads}	ΔE_{ZPE}	$T\Delta S$	ΔG (U=1.23 V)
$*+O_2$	-1259.502	-1247.983	-	-	-	0
$*O_2$	-1258.872	-1247.983	4.303	0.138	0.181	0.63
$*O_2+*H$	-1263.014	-1247.983	3.429	0.414	0.213	-0.198
*OOH	-1263.406	-1247.983	3.068	0.517	0.075	-0.349
$*H_2O_2$	-1268.37	-1247.983	1.314	0.812	0.165	-0.497

Table S7. Detailed adsorption energy (E_{ads}), zero point energy (ΔE_{ZPE}), entropy contribution ($T\Delta S$) and free energy (ΔG) of CN/WO under 0.6 e/Å electric field in ORR process (Unit: eV).

Adsorbate	E_{total}	E_*	E_{ads}	ΔE_{ZPE}	$T\Delta S$	ΔG (U=1.23 V)
$*+O_2$	-1260.604	-1248.943	-	-	-	0
$*O_2$	-1260.097	-1248.943	4.303	0.138	0.181	0.507
$*O_2+*H$	-1264.262	-1248.943	3.429	0.414	0.213	-0.486
*OOH	-1264.743	-1248.943	3.068	0.517	0.075	-0.726
$*H_2O_2$	-1269.593	-1248.943	1.314	0.812	0.165	-0.76

Table S8. Detailed adsorption energy (E_{ads}), zero point energy (ΔE_{ZPE}), entropy contribution ($T\Delta S$) and free energy (ΔG) of CN/WO under 0.8 e/Å electric field in ORR process (Unit: eV).

Adsorbate	E_{total}	E_*	E_{ads}	ΔE_{ZPE}	$T\Delta S$	ΔG (U=1.23 V)
$*+O_2$		-1250.332	-	-	-	0
$*O_2$	-1261.675	-1250.332	4.303	0.138	0.181	
$*O_2+*H$	-1266.103	-1250.332	3.429	0.414	0.213	-0.938
*OOH	-1266.622	-1250.332	3.068	0.517	0.075	-1.216
$*H_2O_2$	-1271.063	-1250.332	1.314	0.812	0.165	-0.841

Table S9. Detailed adsorption energy (E_{ads}), zero point energy (ΔE_{ZPE}), entropy contribution ($T\Delta S$) and free energy (ΔG) of CN/WO under 1 e/Å electric field in ORR process (Unit: eV).

Adsorbate	E_{total}	E_*	E_{ads}	ΔE_{ZPE}	$T\Delta S$	ΔG (U=1.23 V)
$*+O_2$		-1252.446	-	-	-	0
$*O_2$	-1263.723	-1252.446	4.303	0.138	0.181	
$*O_2+*H$	-1268.318	-1252.446	3.429	0.414	0.213	-1.039
*OOH	-1269.163	-1252.446	3.068	0.517	0.075	-1.643
$*H_2O_2$	-1273.168	-1252.446	1.314	0.812	0.165	-2.062

References

1 D. Zhao, C. Dong, B. Wang, C. Chen, Y. Huang, Z. Diao, S. Li, L. Guo and S. Shen, *Adv. Mater*., 2019, 31, 1903545.

2 D. Zhao, Y. Wang, C. Dong, Y. Huang, J. Chen, F. Xue, S. Shen and L. Guo, *Nat. Energy*, 2021, 6, 388-397.

3 Z. Zhang, J. Huang, Y. Fang, M. Zhang, K. Liu and B. Dong, *Adv. Mater*., 2017, 29, 1606688.

4 G. Kresse and J. Furthmüller, *Phys. Rev. B*, 1996, 54, 11169–11186.

5 G. Kresse and J. Furthmüller, *Comp. Mater. Sci.*, 1996, 6, 15–50.

6 J. P. Perdew, K. Burke and M. Ernzerhof, *Phys. Rev. Lett*., 1997, 77, 18, 3865–3868.

7 S. Grimme, J. Antony, S. Ehrlich and H. Krieg, *J. Chem. Phys*., 2010, 132, 154104.

8 S. Grimme, S. Ehrlich and L. Goerigk, *J. Comput. Chem*., 2011, 32, 1456-1465.

9 J. K. Nørskov, J. Rossmeisl, A. Logadottir, L. Lindqvist, J. R. Kitchin, T. Bligaard and H. Jónsson, *J. Phys. Chem. B*, 2004, 108, 17886–17892.

10 M. Wang, X. Dong, Z. Meng, Z. Hu, Y. Lin, C. Peng, H. Wang, C. Pao, S. Ding, Y. Li, Q. Shao and X. Huang, Angew. Chem., Int. Ed., 2021, 60, 11190-11195.

11 S. Guo, H. Zhang, Y. Chen, Z. Liu, B. Yu, Y. Zhao, Z. Yang, B. Han and Z. Liu, *ACS Catal*., 2018, 8, 4576-4581.

12 N. Zhang, X. Li, H. Ye, S. Chen, H. Ju, D. Liu, Y. Lin, W. Ye, C. Wang, Q. Xu, J. Zhu, L. Song, J. Jiang and Y. Xiong, *J. Am. Chem. Soc*., 2016, 138, 8928–8935.